ADVANCED MATERIALS
www.advmat.de

Thermionic Emission in Artificially Structured Single-Crystalline Elemental Metal/Compound Semiconductor Superlattices

*Rahul Singh Rawat, Dheemahi Rao, Sourav Rudra, Nilesh Raut, Bidesh Biswas, Renuka Karanje, Prasanna Das, Ashalatha Indiradevi Kamalasanan Pillai, Je-Hyeong Bahk, Magnus Garbrecht, and Bivas Saha**

Metal/semiconductor superlattices represent a fascinating frontier in materials science and nanotechnology, where alternating layers of metals and semiconductors are precisely engineered at the atomic and nano-scales. Traditionally, epitaxial metal/semiconductor superlattice growth requires constituent materials from the same family, exhibiting identical structural symmetry and low lattice mismatch. Here, beyond this conventional constraint, a novel class of epitaxial lattice-matched metal/semiconductor superlattices is introduced that utilizes refractory hexagonal elemental transition metals and wide-bandgap III-nitride semiconductors. Exemplified by the Hf/AlN superlattices exhibiting coherent layer-by-layer epitaxial growth, cross-plane thermionic emission is observed through current–voltage measurements accomplished for the first time in any metal/semiconductor superlattices. Further, thermoreflectance measurements reveal significant enhancement in cross-plane Seebeck coefficients attributed to carrier energy filtering by Schottky barriers. Demonstration of artificially structured elemental-metal/wide-bandgap compound-semiconductor superlattices promises to usher in new fundamental physics studies and cutting-edge applications such as tunable hyperbolic metamaterials, quantum computing, and thermionic-emission-based thermoelectric and thermophotonic energy conversion devices.

1. Introduction

Epitaxial semiconductor superlattices have been researched extensively to explore fundamental physics and unlock a wide array of new electronic and optoelectronic device applications.[1,2] However, unlike semiconductor superlattices, single crystalline metal/semiconductor superlattices offering unique electronic,[3,4] optical,[5,6] and thermal properties[7,8] distinct from their individual components have been relatively unexplored. Metal/semiconductor superlattices offer several advantages compared to semiconductor superlattices, e.g., the integration of metals introduces unique electronic properties, for instance, plasmonic effects, which can significantly enhance light-matter interactions and enable hyperbolic optical metamaterials.[5,6,9] Similarly, the higher electrical conductivity of metals allows for efficient charge transport across the superlattice structure, which is particularly beneficial for high-speed electronic devices or low-resistance interconnects.[10] Moreover, metals can broaden the range of achievable band alignments and energy levels within the superlattice, offering greater flexibility in tailoring electronic band structures for device applications.[11] Overall, metal/semiconductor superlattices and hetero nanostructures expand the design space and enable the realization of advanced functionalities in both electronics and plasmonics which are not readily achievable with individual metals, semiconductors, or semiconductor superlattices alone.[12–17]

R. S. Rawat, D. Rao, S. Rudra, B. Biswas, R. Karanje, P. Das, B. Saha
Chemistry and Physics of Materials Unit
Jawaharlal Nehru Centre for Advanced Scientific Research
Bangalore 560064, India
E-mail: bsaha@jncasr.ac.in

R. S. Rawat, D. Rao, S. Rudra, B. Biswas, R. Karanje, P. Das, B. Saha
International Centre for Materials Science
Jawaharlal Nehru Centre for Advanced Scientific Research
Bangalore 560064, India

The ORCID identification number(s) for the author(s) of this article can be found under https://doi.org/10.1002/adma.202413537

DOI: 10.1002/adma.202413537

N. Raut, J.-H. Bahk
Department of Mechanical and Materials Engineering
University of Cincinnati
Cincinnati, Ohio 45221, USA

A. I. K. Pillai, M. Garbrecht
Sydney Microscopy and Microanalysis
The University of Sydney
Sydney, NSW 2006, Australia

B. Saha
School of Advanced Materials (SAMat)
Jawaharlal Nehru Centre for Advanced Scientific Research
Bangalore 560064, India

Despite its enormous potential, the deposition of epitaxial metal/semiconductor superlattices presents formidable challenges due to the significant disparities in lattice constants, crystal structures, and growth mechanisms between metals and semiconductors (see Section S1 in the Supporting Information).[13,18,19] Achieving epitaxy, crucial for maintaining desired structural and electronic properties, is impeded by the mismatched lattice parameters of metals and semiconductors, leading to strain-induced defects and dislocation at the interfaces during growth.[20,21] Additionally, metals' inherent chemical reactivity and surface roughness due to high surface energy hinder the formation of smooth and abrupt interfaces.[18]

Yet, despite these challenges, the efforts to develop epitaxial metal/semiconductor heterostructures can be traced back to the late 1960s, when semiconductor superlattices such as GaAs/AlAs were also developed.[22] Nonetheless, it was not until the early 2000s that lattice-matched metal/semiconductor heterostructures were partially realized, primarily within the arsenide family of materials, exemplified by the ErAs/InGaAs system.[23] Subsequently, significant progress emerged in the last decade, particularly with rocksalt nitrides such as TiN/$Al_{0.72}Sc_{0.28}N$ metal/semiconductor superlattices.[5] Rocksalt HfN/ScN,[20] ZrN/ScN,[24] and TiN/$Al_{0.72}Sc_{0.28}N$ superlattices[25] have demonstrated cubic epitaxial growth on (001) MgO substrates, ensuring stability even at elevated temperatures. These superlattices exhibit a myriad of fascinating properties, including exceptional mechanical hardness,[26] intriguing optical hyperbolic photonic dispersion,[5] and substantial enhancement of photonic density of states.[27,28] Moreover, they enable the manipulation of phonon transport and harness phonon wave effects,[8] showcasing their immense potential in diverse technological applications.

However, despite these intriguing advancements, reproducible demonstration of cross-plane electronic transport and thermionic emission in rocksalt nitride metal/semiconductor superlattices have not been achieved. Cross-plane electronic transport consistently exhibits linear current–voltage (*I*–*V*) characteristics in these metamaterials despite the well-defined separation of individual semiconductor layers from the metals within the superlattice.[13,29] Careful analysis shows that these superlattices' non-thermionic electronic nature stems from the semiconductors' high carrier concentration, typically in the $\approx 10^{19}$–10^{20} cm^{-3} range.[24] Such high concentration results in a significantly reduced depletion width of less than 2–3 nm at the metal/semiconductor interface, facilitating electron tunnelling through the Schottky barrier.[24] Notably, rocksalt nitride semiconductors like ScN, CrN, and ErN, along with their rocksalt alloys with conventional III-nitrides such as $Al_{1-x}Sc_xN$, exhibit degenerate semiconducting behavior with large electron concentrations due to the presence of oxygen as impurities and nitrogen vacancies.[30] Consequently, achieving lower carrier concentrations poses a formidable challenge. Therefore, there is a pressing need for alternative material systems capable of yielding epitaxial single-crystalline metal/semiconductor superlattices, wherein wide bandgap semiconductors with low carrier concentrations serve as components, promising new avenues for the exploration of fundamental physics and a new generation of devices.

A novel and unexplored materials system with great potential for epitaxial metal/semiconductor superlattice heterostructure growth involves hexagonally close-packed (*hcp*) elemental transition and rare-earth metals in conjunction with compound III-nitride wurtzite semiconductors, such as AlN, GaN, and InN. Refractory *hcp* metals such as Ti, Zr, and Hf are stable in ambient conditions and exhibit high mechanical hardness, lustrous appearance, and excellent electrical and thermal conductivities.[31] Moreover, in addition to their similar crystal structures, several *hcp* metals closely match the in-plane (*a*) and out-of-plane (*c*) lattice constant of III-nitride semiconductors. Illustrating this compatibility (see **Figure 1a**), an analysis of 25 different *hcp* metals (transition and rare-earth) reveals the remarkably minimal lattice mismatch with wide bandgap wurtzite III-nitrides. For example, AlN exhibits a 2.5% and 1.4% mismatch in *a* and *c*, respectively with Hf (see Section S2 and Figure S2a,b, Supporting Information), while GaN demonstrates nearly perfect matching with Mg and ≈3.3% and 1.7% mismatch in *a* and *c*, respectively with Sc (see Section S2 and Figure S2c,d, Supporting Information). Similarly, in narrow bandgap semiconductors, InN presents a small mismatch with rare-earth metals such as Gd, Er, and Ho (see Section S2 and Figure S2e,f, Supporting Information).

Remarkably, the lattice parameter on the (111) plane of the rocksalt metal nitrides such as HfN, ZrN, and ScN also matches well with the *a* of the *hcp* metals, further ensuring epitaxial retention even if nitridation of the initial few metal layers during the superlattice growth becomes inevitable (see Section S2 and Figure S2, Supporting Information). Therefore, regarding crystal structure similarities and lattice-matching, *hcp* metals meet the established criteria for epitaxial, single-crystalline superlattice development with wurtzite III-nitride semiconductors.

It is noteworthy that while many of the transition and rare-earth metals maintain an *hcp* crystal structure at room temperature and above, some may also adopt other structural symmetries when deposited at elevated temperatures.[32] Hence, with meticulous control over growth conditions, the deposition of *hcp* elemental metal/wide bandgap wurtzite semiconductor single-crystalline superlattices (as in Figure 1b), showcasing many intriguing properties, should be achievable. In this work, we present the inaugural experimental demonstration of an archetypical Hf/AlN metal/semiconductor superlattice system exhibiting thermionic emission and electron energy filtering. This achievement is notable for not only challenging conventional material choice criteria but also for overcoming the significant hurdles previously encountered in cross-plane electrical measurements of rocksalt nitride metal/semiconductor superlattices.

2. Results and Discussion

Epitaxial Hf/AlN metal/semiconductor superlattices are deposited inside an ultrahigh vacuum (UHV) magnetron sputtering system at a base pressure of 1×10^{-9} Torr (see Section S3, Supporting Information for details) on (0001) Al_2O_3 substrates. A 50 nm AlN buffer layer is deposited initially at 800 °C substrate temperature to reduce the lattice mismatch with the (0001) Al_2O_3 substrate and promote epitaxial growth. Subsequently, the Hf/AlN superlattices are deposited at 500 °C to ensure that the Hf layers retain their *hcp* crystal structure (see Section S7, Supporting Information). Symmetric 2θ-ω X-ray diffractogram shows that the Hf/AlN superlattices grow with (0002) orientations on (0001) Al_2O_3 substrates forming a nominal single-crystalline

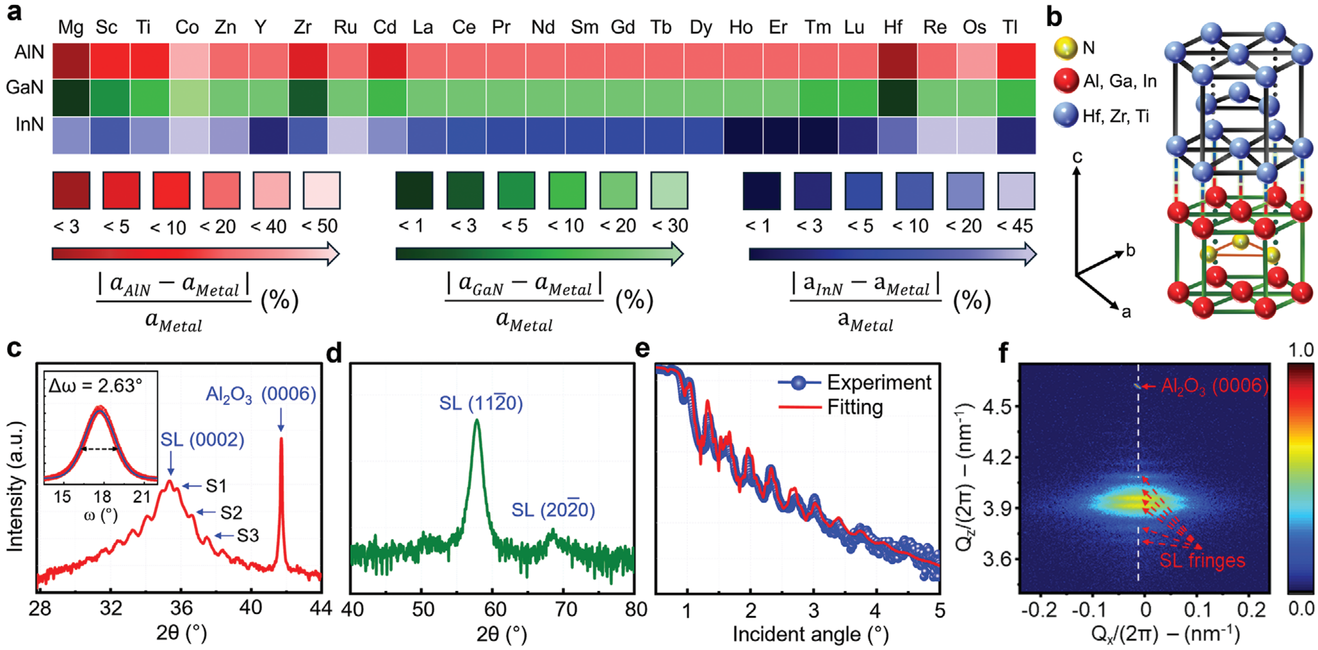

Figure 1. Growth and structural characterization of Hf/AlN metal/semiconductor superlattice. a) A list of 25 different elemental transition and rare-earth metals exhibiting hexagonal crystal structure and traditional wurtzite III-nitride semiconductors are shown along with the mismatches in their in-plane lattice constant (*a*) in a colour schematic. The colour contrast scales identify the closely lattice-matched metal/semiconductor combination. b) The schematic crystal structure and unit cell of the hexagonal elemental metal/III-A semiconductor superlattices. c) Symmetric 2θ-ω X-ray diffraction pattern of Hf/AlN superlattices deposited on (0001) Al_2O_3 substrates with 50 nm AlN buffer layer. Interference fringes are visible along with the main (0002) superlattice diffraction peak. d) The in-plane XRD of the superlattices showing the diffraction peaks from (11$\bar{2}$0) and (20$\bar{2}$0) planes of Hf/AlN superlattices. e) X-ray reflectivity (XRR) of the superlattice, showing sharp Kiessig fringes that highlight atomically sharp and abrupt interfaces. f) X-ray reciprocal space map (RSM) of the superlattices showing pseudomorphic growth and interference fringes that evidence the nominally single-crystalline and epitaxial nature of the superlattices.

heterostructure (see Figure 1c). Along with the main 0002 diffraction peak, several superlattice reflections are visible on both sides of the main peak, suggesting coherent layer-by-layer growth. The ω-scan (rocking curve) corresponding to the (0002) diffraction planes exhibit (see inset in Figure 1c) a full-width-at-the-half-maximum (FWHM) of 2.6°. An out-of-plane lattice constant (*c*) of 5.05Å is determined for the superlattices from the 2θ-peak position, close to the *c*-axis lattice parameter of Hf (5.06Å) and AlN (4.98Å). Further, the in-plane XRD measurements show diffraction peaks from the (11$\bar{2}$0) and (20$\bar{2}$0) planes (see Figure 1d), yielding an *a* of 3.18Å in superlattices that is nearly the same as the *a* of Hf (3.18 Å) and AlN (3.11 Å) (see Section S6A, Supporting Information for more details).

X-ray reflectivity (XRR) measurements show Kiessig fringes due to the interference of X-rays from different interfaces (see Figure 1e). Fitting of the XRR yields an individual Hf and AlN layer thickness of 13 and 10 nm, respectively, which match well not only with the period thickness measured from the 2θ-seperation (22 nm) of the superlattice reflections (see in Figure 1c) but also with the intended thickness during growth. Interestingly, the XRR fittings also reveal that the interface roughness increases slightly with the increasing number of periods (see Section S6B, Supporting Information) and exhibits an average Hf/AlN and AlN/Hf interface roughness of 0.86 and 0.77 nm, respectively. These roughness's are comparable to the interface roughness of previously developed epitaxial $TiN/Al_{0.72}Sc_{0.28}N$ superlattices.[5] The reciprocal space X-ray mapping (RSM) further shows that the (0001) Al_2O_3 substrate and the superlattice diffraction peaks are all aligned vertically at the same Q_x, which verifies the pseudomorphic growth (see Figure 1f). A slight spread (ΔQ_x) of the main superlattice peak and interference fringes in the RSM indicates a residual strain in the heterostructure. From this XRD analysis, an epitaxial relationship of [0001] (0002) SL || [0001] (0006) Al_2O_3 is determined for the Hf/AlN superlattices.

The structure of the superlattices are further analysed with high-resolution (scanning) transmission electron microscopy (HR(S)/TEM), which shows distinctly separated Hf and AlN layers (see **Figure** 2a). The bottom AlN buffer layer is used to reduce the lattice mismatch between superlattice and substrate. Yet, some threading dislocations originating at the AlN/Al_2O_3 interface traverse to the superlattice causing a light bending of the layers around these dislocations and a slight wavy nature of the layers as seen previously in nitride superlattices.[24] The electron diffraction pattern (see inset in Figure 2a) measured along the [11$\bar{2}$0] direction shows two sets of diffraction spots originating from the superlattice and the substrate. The high-angle annular dark field scanning transmission electron microscopy (HAADF-STEM) imaging shows vivid contrast difference between the heavy Hf and relatively lighter AlN and visualizes the interfaces roughening quantified earlier with XRR (see Figure 2b). Additionally, the AlN/Hf interfaces are slightly sharper compared to the Hf/AlN interfaces. This difference arises because the surface energy of Hf is lower than that of AlN (refer to Section S4A,

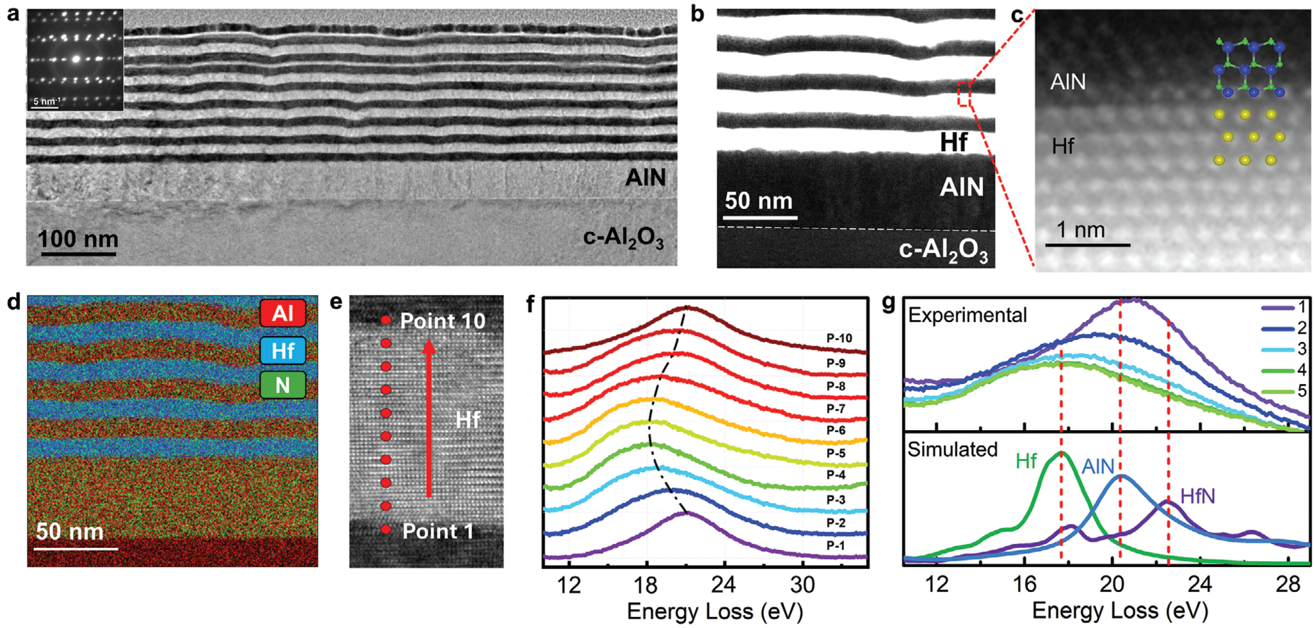

Figure 2. High-resolution transmission electron microscopy imaging of Hf/AlN metal/semiconductor superlattices. a) TEM micrograph of Hf/AlN superlattice showing distinct layer-by-layer Hf and AlN growth on AlN buffer layer deposited on *c*-Al_2O_3. The electron diffraction pattern of the superlattice consists of two sets of diffraction spots corresponding to the superlattice and the substrate. b) HAADF-STEM micrograph of the superlattice reveals wavy layers bending around the threading dislocations originating at the AlN/*c*-Al_2O_3 interface and high brightness contrast among the Hf and AlN layers. c) Atomic-resolution imaging of Hf/AlN superlattice at the interface, marked with ABAB hexagonal stacking in Hf layers as shown by the golden colour Hf atoms. The AlN layer appears to begin with an Al-terminated plane (blue colour of Al atoms) bonded with nitrogen in green colour. d) STEM-EDS map of the Hf, Al, and N shows the distribution of different elements in the superlattice. The micrograph shows Hf and Al atoms are well-separated. e) HAADF-STEM micrograph of Hf layer showing 10 different points, where individual EELS spectra were collected. f) The EELS spectra at the 10 marked points corresponding to the unscreened plasmon exaction are presented. g) The systematic shift of the EELS peak from higher energy at point 1 (Hf/AlN interface) to lower energy at point 5 (centre of Hf layer) matches with the simulated bulk plasmon peaks suggesting slight nitridation at the interface. With respect to the interfaces, the core of the Hf layer contains a lesser amount of diffused nitrogen.

Supporting Information). Consequently, Hf tends to wet AlN layers more readily than the reverse, leading to the observed asymmetric roughening of the interfaces.

The atomic-resolution STEM image at the Hf/AlN interface clearly shows the atomic staking (see Figure 2c). The ABAB stacking sequence along the [0002] of Hf is clearly indicated by golden colour spheres. On top of the Hf layer, the AlN layer begins with an Al-terminated plane (blue spheres), while nitrogen appears as a faint streak above it (small green spheres) due to the lower Z-contrast of nitrogen atoms in the dark field mode of STEM. The TEM-energy dispersive X-ray spectroscopy (EDS) elemental mapping further shows distinct individual layers without appreciable intermixing between Hf and Al atoms (see Figure 2d; Figure S20, Supporting Information). However, nitrogen appears to diffuse during the growth process into the Hf layer, and the Hf layer exhibits a relatively higher concentration of unintentional oxygen due to higher degrees of oxygen present in the target (see Section S6C, Supporting Information). Despite the presence of oxygen and nitrogen, the hexagonal crystal structure is retained suggesting no significant effect of these impurities on the superlattice quality.

While the HRXRD and microscopy analysis establishes the excellent structural quality of the superlattices, the nitrogen diffusion inside the Hf layers during the growth either from residual nitrogen background pressure or from the adjacent AlN layers is investigated in detail. Electron energy loss spectroscopy (EELS) point-scans recorded across a representative Hf layer (see Figure 2e) show inelastically scattered electron energy loss peaks corresponding to the unscreened plasmons. Notably, the EELS peak at 17.7 eV at the centre of the Hf layer (point 5) shifts gradually toward higher energies near the interface regions (point 1 and point 10) as shown in Figure 2f. Such blue shifts of the EELS peak near the interface indicate some Hf bonding with diffused nitrogen from the adjacent AlN layers. The experimental spectra are compared with the first-principles simulated spectra as in Figure 2g (see Section S4D, Supporting Information for simulation details). Near the interface (point 1 and point 10) AlN contribution is also present as observed from the simulated data while the central layer is mostly elemental Hf. Additionally, our EELS simulation of some stable Hf-Al binary intermetallics[33] discards the possibility of the formation of an appreciable amount of such Hf-Al binary compound near the interface (see Section S4D, Supporting Information for details), which could otherwise significantly alter the band offset and barrier height. Also, compositional analysis from XPS shows the formation of distinct elemental Hf metal and compound AlN semiconductor in the superlattice (see Section S6D, Supporting Information for details).

Further, to differentiate the Hf/AlN superlattices from an unlikely HfN/AlN heterostructure formation due to the nitrogen diffusion in Hf layers, separate HfN/AlN superlattices are deposited on (0001) Al_2O_3 substrates. Structural characterization (see section S7, Supporting Information) reveals that although

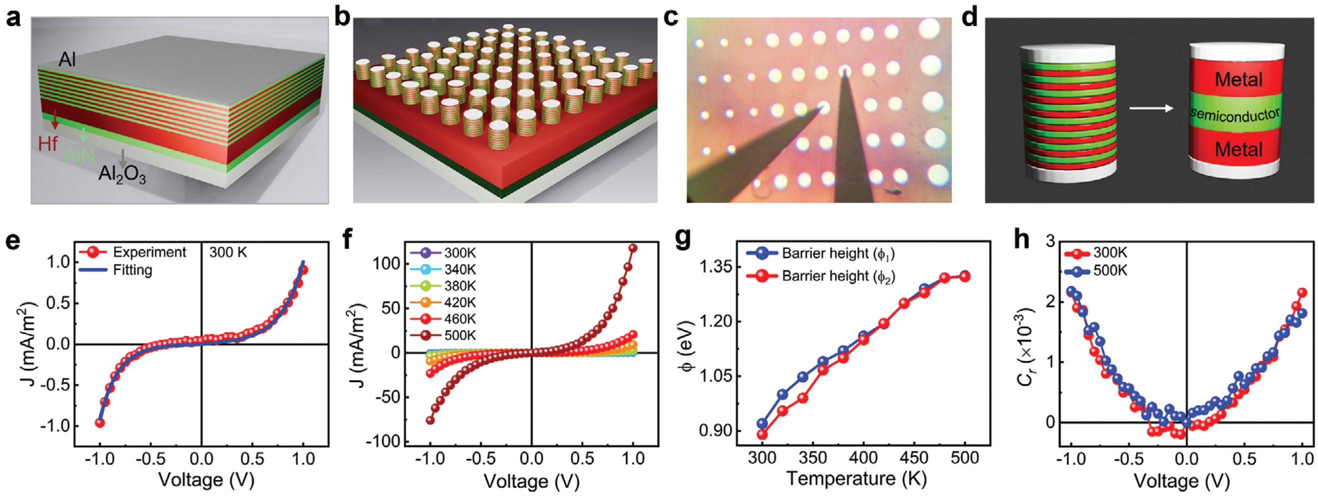

Figure 3. Electrical characterization of Hf/AlN superlattice devices. a) Schematic of Hf/AlN metal/semiconductor superlattice with bottom Hf metallic layer and top aluminium layer. b) The schematic of superlattice devices after the nanofabrication and etching process. c) The optical image of the devices during the electrical measurements. d) The *I–V* characteristics of the measured superlattice structure are modelled by considering the superlattice as an effective medium consisting of a single metal/semiconductor/metal structure with one forward and one backward Schottky diode. e) Room-temperature *I–V* characteristics of the Hf/AlN superlattice exhibit a symmetric nature. The measured *I–V* curve is fitted with the analytically calculated *I–V* expression for an MSM diode, as shown in Equation 1 f) Temperature-dependent *I–V* characteristics of the superlattice show an increase in the device current at higher temperatures. g) Temperature-dependent barrier height extracted from the *I–V* characteristics of superlattice. Barrier height increases with increasing temperature due to the inhomogeneous distribution of barrier height. h) *CV* characteristics of superlattice devices, where the relative capacitance (C_r) is defined as $(C_V\text{-}C_0)/C_0$.

the individual HfN and AlN layers are well-separated, HfN/AlN superlattice interfaces are much wavey and relatively diffused. Although the lattice constant on the (111) plane of HfN is closely matched with the "*a*" of AlN, mismatches in the crystal structure between HfN and AlN layers lead to dislocations and planar defects. These results further confirm the role of structural symmetry and lattice-matching in the superlattice growth and the superior crystallinity of Hf/AlN metal/semiconductor superlattices. A recent discovery from Wang et al. demonstrated the formation of Mg intercalated Mg/GaN superlattice.[14] The intercalation of Mg was possible due to the very small lattice mismatch between Mg and GaN in both in-plane and out-of-plane directions. While we have demonstrated growth and thermionic emission in Hf/AlN metal/semiconductor superlattices, other epitaxial metal/semiconductor superlattices such as Mg/GaN, Sc/GaN, Gd/InN, and Er/HfN can be formed utilizing the strategy presented in this work.

While the structural characterization showcases the inaugural demonstration of the *hcp* elemental metal/wide-bandgap III-nitride semiconductor superlattices, the conclusive demonstration of thermionic emission elevates it to the first of its kind. For the cross-plane transport measurements, Hf/AlN superlattices are deposited on the 80 nm-Hf/50 nm-AlN/ buffer layer on (0001) Al_2O_3 substrates, serving as the back metallic plate for current flow. A series of nanofabrication, etching, and metallization processes (as detailed in Section 3F, Supporting Information) is used to create superlattice pillars with eight-period superlattices having variable diameters (see **Figure 3**a,b). Current–voltage (*I–V*) and capacitance-voltage (*CV*) measurements are performed across sets of different pillars with the current path going through 16 (2× number of periods) back-to-back forward and backward Schottky diodes placed in a series in each pillar and through the bottom Hf metallic layer (see Figure 3c). Measurements are performed inside a probe station with a vacuum chamber at 1×10^{-6} Torr. in 2-probe measurement geometry (see Section 3G, Supporting Information for measurement details).

Room-temperature cross-plane electrical measurement shows near-symmetric Schottky diode *I–V* characteristics for the Hf/AlN superlattices (see Figure 3e). To fit the *I–V* curve and extract diode characteristics, the measured superlattice stack is assumed to be an effective metal-semiconductor-metal (MSM) Schottky diode medium having forward and backward barrier heights φ_1 and φ_2, and ideality factors η_1 and η_2, respectively,[34] as shown in Figure 3d. The *I–V* characteristics of such an MSM Schottky diode can be expressed as (see Section S3H, Supporting Information for the details).

$$J(V) = \frac{2.J_{01}.J_{02}.sinh\left(\frac{eV}{2k_BT}\right)}{J_{01}e^{\frac{eV}{2k_BT}} + J_{02}e^{-\frac{eV}{2k_BT}}} \tag{1}$$

where

$$J_{01,02} = AT^2 \exp\left(-\frac{\varphi_{B1,2}}{k_BT}\right) \tag{2}$$

J_{01} and J_{02} are the reverse saturation current density, *A* is the Richardson constant (4.67×10^5 $Am^{-2}K^{-2}$), *T* is temperature, $k_B = 1.38 \times 10^{-23}$ J K^{-1} is the Boltzmann constant, *e* is the charge of the electron (1.602×10^{-19} C), $\varphi_{B1,2}$ are the Schottky barrier heights, and *V* is the applied voltage. The deviation from the ideal behavior is accounted for with the ideality factor η in

$$\varphi_{B1,B2}(V) = \varphi_{B01,B02} \pm eV_{1,2}\left(1 - \frac{1}{\eta_{1,2}}\right) \tag{3}$$

Equation 1 fits the experimentally measured $I–V$ characteristics very well and yields room-temperature φ_1 and φ_2 of 0.92 eV and 0.89 eV, respectively (see Figure 3e) with J_{01} and J_{02} being 4.38 $\times$ 10^{-6} A m^{-2} and 1.45 $\times$ 10^{-5} A m^{-2}, respectively. The fittings are satisfactory with goodness of fit measured by R-square always greater than 0.98. Further, η_1 and η_2 of 1.4 and 1.3 are extracted from the fittings, suggesting the high-quality Schottky diode behavior of Hf/AlN superlattices. Though the barrier heights and ideality factors should be ideally the same for forward and backward diodes, the growth and nanofabrication process lead to small asymmetry in the interface characteristics that cause such tiny variations. The $I–V$ characteristics and the barrier heights are consistent across various measurements and devices (see Section S10, Supporting Information).

According to the Mott-Schottky equation, the barrier height (φ_B) can be determined from the work function of metal (ψ) and electron affinity of semiconductor (χ) as $\varphi_B = \psi - \chi$.[35] Hf exhibits a work function of 3.9 ± 0.1 eV,[36] and the electron affinity of AlN is debated to be in the 0.6–2.1 eV range,[37,38] yielding a barrier height in a wide range from 3.3–1.8 eV from the Mott-Schottky equation. Nevertheless, the measured Schottky barrier height of Hf/AlN interfaces is significantly smaller compared to the Mott-Schottky predictions. Such a smaller Schottky barrier height suggests pinning of the Fermi level inside the bandgap of AlN due to the presence of interface-induced gap states (IFIGS) and defect states from the nitrogen-vacancy, charge transfer, and dipole and image charge formation which was observed previously for other metal/compound semiconductor heterojunctions.[39–41] The first-principles simulated valence band offset and the presence of surface states within the bandgap of the Al-terminated AlN evidences the possibility of Fermi level pinning (see Section S4B,C, Supporting Information for details).

Temperature-dependent measurements show that the $I–V$ curves remain similar to that of the room temperature, albeit with increased device current with temperature in the 300–500 K range (see Figure 3f). Fitting of the temperature-dependent $I–V$ curves with Equation 1 shows a linear increase in the barrier heights, with φ_1 increasing from 0.92 to 1.3 eV and φ_2 from 0.89 to 1.32 eV with increasing temperature from 300 to 500 K (see Figure 3g). As shown in Figure 3f, the current increases nearly exponentially with the temperature at a fixed voltage due to the increased thermal excitation of carriers to go over the barrier. Yet the increasing barrier height with temperature mitigates the effect, reducing the rate of increase in current with temperature. Such an increase in the barrier height with temperature originates due to the barrier inhomogeneities[42–44] (see section S8, Supporting Information for details), allowing the higher barrier height regions to be activated at elevated temperatures. Fitting of the temperature-dependent barrier height with a functional relationship as in Equation (4) yields an $\overline{\varphi_B} = 1.969$ eV and $\sigma_s =$ 234.4 mV for the forward and reverse junction $\overline{\varphi_B} = 2.016$ eV and $\sigma_s = 242.9$ mV in the 300–500 K temperature range, consistent with GaN Schottky diodes.[45]

$$\varphi_B = \overline{\varphi_B} - \frac{e^2\sigma_s^2}{2k_BT}, \tag{4}$$

where φ_B is barrier height extracted from $I–V$ curve fitting, $\overline{\varphi_B}$ is mean barrier height, T is temperature, σ_s is the standard deviation of barrier height, and k_B is the Boltzmann constant.

Further, CV measurement of the superlattices shows voltage dependency of capacitance, where the device capacitance increases with increasing the *dc*-bias (V) (see Section S9, Supporting Information). Such voltage dependence of capacitance, increasing C with V ($dC/dV > 0$) is a common feature of MSM diodes, previously also seen in other material systems.[46,47] Although the origin of such capacitance behavior is strongly debated, the presence of trap states near the metal-semiconductor interface and space charges accumulation near the electrodes giving rise to a double-layer capacitance, referred to as electrode polarization and nonlinearities of the bond polarizability are predicted to cause such behavior. Nevertheless, the CV characteristics fit with Equation 5 very well.[48]

$$\Delta C/C_0 = \alpha V + \beta V^2 \tag{5}$$

where C_0 is the capacitance at zero bias, $\Delta C = C_V - C_0$, β and α are the linear and quadratic coefficients of capacitance. At room temperature fitting the CV curve with Equation 5 yields an α and β of 63.17 μV^{-1} and 2.381 mV^{-2}, respectively (see Figure 3h). Moreover, temperature-dependent measurements reveal that the quadratic nature of the CV curves remains unaltered at higher temperatures up to 500 K (Figure 3h).

An important consequence of the thermionic emission in metal/semiconductor superlattices is the Seebeck coefficient enhancement along the cross-plane direction, the prediction of which has fuelled its interest in recent years.[49–51] Therefore, the cross-plane Seebeck coefficient of the Hf/AlN superlattices is measured with the thermoreflectance imaging (TRI) technique (see Section S12, Supporting Information for method details).[52] In this method, the bottom of the substrate is heated using a thermoelectric module to create temperature gradients across the superlattice in the cross-plane direction. As shown in **Figure 4**a, the TRI images capture small temperature differences up to a few degrees created between the top of the 50 µm circular superlattice device and the etched surrounding area that reveals the bottom Hf electrode. The voltage created between the two regions due to the Seebeck effect was simultaneously measured using a DC voltmeter under no current flow. The voltage (ΔV) varies linearly with varying temperature (ΔT) as in Figure 4b with a slope yielding the Seebeck co-efficient of 140.05 ± 6.28 µV K^{-1}. Figure 4c represents the temperature in the region of interest (ROI) on the superlattice where the temperatures are averaged for the same device. The Gaussian distribution indicates the statistical spread of the measured reflectivity data, ensuring the measurements are not biased, and highlighting the central tendency and the low variability of the data.

The bare Hf sample shows the Seebeck coefficient of ≈4 µV K^{-1} near room temperature with the positive sign. The positive Seebeck coefficient of such a small magnitude is typical for metals having non-ideal free electron density of states near the Fermi level with the complicated Fermi surface touching the Brillouin zone edge.[53,54] On the other hand, the Hf/AlN superlattices show negative Seebeck coefficients with a much larger magnitude, −133.04 ± 8.26 µV K^{-1} for the 100 µm-diameter device and −140.05 ± 6.28 µV K^{-1} for the 50 µm-diameter

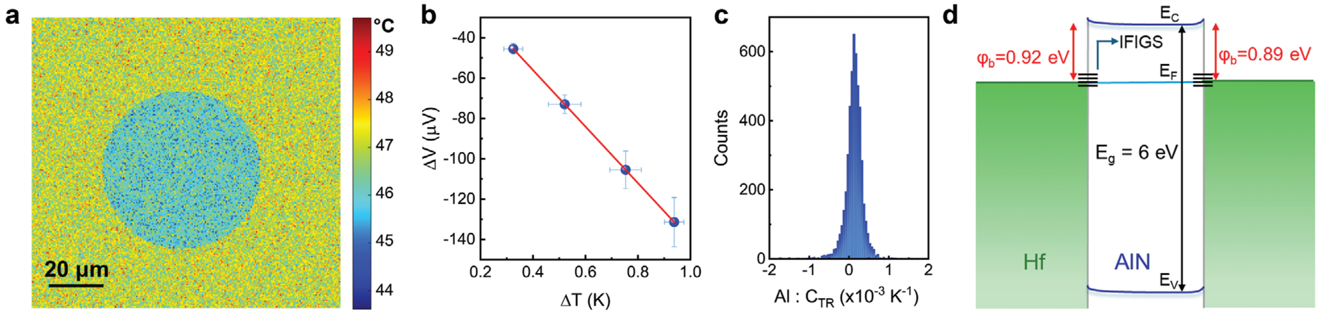

Figure 4. Thermoreflectance imaging (TRI) and Seebeck coefficient of Hf/AlN superlattices. a) Temperature-mapping of the Hf/AlN superlattices 50 μm diameter device obtained with TRI technique. b) The slope of the voltage variation with changes in temperature is fitted to obtain the Seebeck coefficient of 140.05 ± 6.28 μV K^{-1} c) The averaged temperature in ROI on 50 μm Al contact ensures no bias and low variability in the measurement. d) Schematic of the Schottky barrier at the Hf/AlN/Hf interface formed by the Fermi level pinning to the interface-induced gap states.

device, clearly indicating the Seebeck enhancement due to the carrier transport over the barriers, also called the energy filtering effect.[49] The sign change of the Seebeck coefficient from the bare Hf to the superlattices may indicate that the Fermi level is pinned near the conduction band minimum of AlN due to the presence of native O_N and V_N donor defects so that electrons dominate over holes in the thermionic transport in the superlattices. The size dependence of the Seebeck value seems to depend on the rectification ratio of the device which is higher for smaller devices. The larger-area pillars presumably have more leakage current than the smaller-area one due to more defects existing in the larger area, which weaken the energy filtering effects, resulting in a smaller magnitude of the Seebeck coefficient. Figure 4d presents the schematic of the Schottky barrier at the Hf/AlN interface that is responsible for the thermionic emission and hence enhancement in the Seebeck coefficient. More experiments and theoretical studies might be necessary to further investigate this effect. Along with the successful thermionic emission, these hexagonal metal/semiconductor superlattices also exhibit optical hyperbolic dispersion (see Section S11, Supporting Information).

3. Conclusion

In summary, we present a new class of artificially engineered epitaxial metal/semiconductor superlattices that leverage hexagonal elemental transition, or rare-earth metals paired with compound III-nitride wurtzite semiconductors. Epitaxial Hf/AlN metal/semiconductor superlattices, a prime example within this class, demonstrate coherent layer-by-layer growth. Cross-plane transport measurements unveil the thermionic emission behavior of these superlattices, with the Schottky barrier height increasing with rising temperature. Moreover, a quadratic voltage dependence in capacitance aligns with an effective metal-semiconductor-metal capacitor model for the superlattices. The cross-plane Seebeck coefficient enhancement measured with the TRI technique reveals the electron filtering effect by the Schottky barriers. These results mark a significant breakthrough in exhibiting a new class of artificially structured material in elemental metal/compound semiconductor superlattices and showing the first experimental demonstration of thermionic emission in metal/semiconductor superlattices. In this way, our discovery heralds a new era in artificial heterostructures, promising advancements in electronic, plasmonic, and energy conversion devices fuelled by thermionic emission.

4. Experimental Section

Superlattice Growth: Hf/AlN metal/semiconductor superlattices were deposited on (0001) Al_2O_3 substrates (1 cm × 1 cm) inside an ultrahigh vacuum chamber with a base pressure of 1×10^{-9} Torr with a reactive DC magnetron sputtering (PVD Products, Inc.). The substrates were cleaned with wet chemical (acetone and methanol) methods using a sonicator before transferring to the load lock operated at a pressure of $\approx 1 \times 10^{-7}$ Torr. Al (purity of 99.999%) and Hf (purity of 99.95%) targets had a dimension of 2 inches in diameter and 0.25 inch in thickness and sputtered with 100 and 25 W DC-power, respectively. The films were deposited at 10 mTorr pressure, maintaining the Ar:N_2 gas mixture ratio of 9:2 standard cubic centimetres per minute (sccm.). Before growing the superlattice, a 50 nm AlN buffer layer was deposited to reduce the substrate-to-film lattice mismatch. The buffer layer was deposited on (0001) Al_2O_3 substrates at 800 °C. Subsequently, the 10 nm/10 nm Hf/AlN superlattices were deposited at 500 °C. The growth rate of the superlattices was $\approx$1 nm min^{-1}.

Device Fabrication and Measurement: For cross-plane electronic transport measurement, devices were fabricated using optical lithography and reactive ion etching (RIE) processes. An 80 nm Hf bottom metallic layer as a back electrode plate was deposited on a 50 nm AlN buffer layer on (0001) Al_2O_3 substrates before the superlattice growth. Subsequently, 8 periods of 10 nm/10 nm Hf/AlN superlattices were deposited. The superlattice was terminated with the 10 nm Hf layer to protect the surface and provide good electrical contact.

Further, spin coating was used to deposit photoresist and optical lithography was used to create the circular patterns of 50, 100, 150, and 200 μm diameter. Subsequently, 100 nm thick Al metal was evaporated on the superlattice to serve as an electrode. Finally, RIE with CF_4 process gas was used to etch and prepare the superlattice cylindrical pillars. The etching rate was pre-optimized to ensure that the pillars start from the Hf back metallic layer and exhibit a smooth bottom later. Al was utilized as a contact metal due to its dual functionality of acting as a mask for CF_4 etching gas and being the top metal contact.

The electrical transport characteristics of the superlattices were measured in the Keithley 4200 attached to the probe station.

Characterization: The structural characterization of the superlattices was performed with a Rigaku SmartLab X-ray diffraction system consisting of the PhotonMax high-flux 9 kW rotating anode. STEM images and EDS maps were recorded with an image- and probe-corrected and monochromated Themis-Z 60–300 kV equipped with a high-brightness XFEG source and Super-X EDS detector system for ultra-high-count rates, operated at 300 kV. EELS spectra were recorded in STEM mode utilizing a GATAN Quantum ERS 965 GIF with an ultra-fast shutter and Dual EELS system. Thermoreflectance imaging (TRI) was employed with an iterative calibration process to accurately determine the Thermoreflectance coefficient (C_{TR}) for the top contact metal and subsequently, the Seebeck coefficient.

EELS Simulation: The electron energy loss spectrum (EELS) was simulated using the time-dependent density functional perturbation theory (TD-DFPT) approach as implemented in the TURBOEELS code within the Quantum ESPRESSO package.

Supporting Information

Supporting Information is available from the Wiley Online Library or from the author.

Acknowledgements

R.S.R. and B.S. acknowledge the International Centre for Materials Science (ICMS) and Sheikh Saqr Laboratory (SSL) of Jawaharlal Nehru Centre for Advanced Scientific Research (JNCASR) for support. B.S. acknowledges Ras Al Khaimah Centre for Advanced Materials and Raknor LLC for financial support. B.S. acknowledges the Young Scientist Research Award (YSRA) from the Board of Research in Nuclear Sciences (BRNS), Department of Atomic Energy (DAE), India with grant number 59/20/10/2020-BRNS/59020 for partial financial support. R.S.R., D.R., B.B., P.D., and B.S. acknowledge the *SAMat* Research Facilities, JNCASR, Bengaluru. P.D. and S.R. thanks CSIR for the fellowship. R.S.R. thanks JNCASR for the fellowship. S.R., R.K., and B.S. acknowledged the PARAM Yukti supercomputing facility under the national supercomputing mission of India at JNCASR, Bengaluru for providing computational resources. M.G. and A.I.K.P. acknowledge the facilities of Sydney Microscopy and Microanalysis at the University of Sydney.

Conflict of Interest

The authors declare no conflict of interest.

Author Contributions

R.S.R., D.R., S.R. contributed equally to this work. B.S. conceived this project. R.S.R. and B.B. deposited the superlattice films and performed structural characterizations. R.S.R. and D.R. performed the device fabrication and electrical characterization. S.R., R.K., and B.S. performed the theoretical modelling and analysis. A.I.K.P. performed the TEM sample preparation and M.G. performed the TEM imaging, EDS mapping, and EELS data acquisition and analysis. N.R. and J.H.B. perform the TRI measurements and data analysis for the SLs. P.D. and B.S. performed the optical characterization and analysis. All authors discussed and contributed to the preparation of the manuscript.

Data Availability Statement

The data that support the findings of this study are available from the corresponding author upon reasonable request.

Keywords

III-nitride semiconductors, metal/semiconductor superlattices, schottky barrier, seebeck coefficient enhancement, thermionic emission

Received: September 9, 2024
Revised: November 11, 2024
Published online:

[1] L. Esaki, L. L. Chang, *Phys. Rev. Lett.* **1974**, *33*, 495.
[2] L. Esaki, R. Tsu, *IBM J. Res. Dev.* **1970**, *14*, 61.
[3] D. Vashaee, A. Shakouri, *J. Appl. Phys.* **2004**, *95*, 1233.
[4] M. Tanaka, C. J. Palmstrøm, M. Tsuda, T. Nishinaga, *J. Magn. Magn. Mater.* **1996**, *156*, 276.
[5] B. Saha, G. V. Naik, S. Saber, C. Akatay, E. A. Stach, V. M. Shalaev, A. Boltasseva, T. D. Sands, *Phys. Rev. B – Condens. Matter Mater. Phys.* **2014**, *90*, 125420.
[6] G. V. Naik, B. Saha, J. Liu, S. M. Saber, E. A. Stach, J. M. K. Irudayaraj, T. D. Sands, V. M. Shalaev, A. Boltasseva, *Proc. Natl. Acad. Sci. USA.* **2014**, *111*, 7546.
[7] B. Saha, T. D. Sands, U. V. Waghmare, *J. Phys. Condens. Matter.* **2012**, *24*, 415303.
[8] B. Saha, Y. R. Koh, J. P. Feser, S. Sadasivam, T. S. Fisher, A. Shakouri, T. D. Sands, *J. Appl. Phys.* **2017**, *121*, 015109.
[9] P. Das, K. C. Maurya, J. L. Schroeder, M. Garbrecht, B. Saha, *ACS Appl. Energy Mater.* **2022**, *5*, 3898.
[10] D. L. Smith, E. Y. Lee, V. Narayanamurti, *Phys. Rev. Lett.* **1998**, *80*, 2433.
[11] S. Nayak, S. Acharya, M. Baral, M. Garbrecht, T. Ganguli, S. M. Shivaprasad, B. Saha, *Appl. Phys. Lett.* **2019**, *115*, 251901.
[12] J. Henz, M. Ospelt, H. Von Känel, *Surf. Sci.* **1989**, *211*, 716.
[13] B. Saha, A. Shakouri, T. D. Sands, *Appl. Phys. Rev.* **2018**, *5*, 021101.
[14] J. Wang, W. Cai, W. Lu, S. Lu, E. Kano, V. C. Agulto, B. Sarkar, H. Watanabe, N. Ikarashi, T. Iwamoto, M. Nakajima, Y. Honda, H. Amano, *Nature* **2024**, *631*, 67.
[15] T. Sands, C. J. Palmstrøm, J. P. Harbison, V. G. Keramidas, N. Tabatabaie, T. L. Cheeks, R. Ramesh, Y. Silberberg, *Mater. Sci. Reports* **1990**, *5*, 99.
[16] X. Wan, Y. Pan, Y. Xu, J. Liu, H. Chen, R. Pan, Y. Zhao, P. Su, Y. Li, X. Zhang, S. Zhang, H. Li, D. Su, Y. Weng, J. Zhang, *Adv. Mater.* **2023**, *35*, 2207555.
[17] X. Wan, Y. Gao, M. Eshete, M. Hu, R. Pan, H. Wang, L. Liu, J. Liu, J. Jiang, S. Brovelli, J. Zhang, *Nano Energy* **2022**, *98*, 107217.
[18] K. N. Tu, *IBM J. Res. Dev.* **1990**, *34*, 868.
[19] P. Jha, T. D. Sands, L. Cassels, P. Jackson, T. Favaloro, B. Kirk, J. Zide, X. Xu, A. Shakouri, *J. Appl. Phys.* **2012**, *112*, 063714.
[20] M. Garbrecht, J. L. Schroeder, L. Hultman, J. Birch, B. Saha, T. D. Sands, *J. Mater. Sci.* **2016**, *51*, 8250.
[21] S. Rudra, D. Rao, S. Poncé, B. Saha, *Nano Lett.* **2023**, *23*, 8211.
[22] R. Merlin, K. Bajema, R. Clarke, F. Y. Juang, P. K. Bhattacharya, *Phys. Rev. Lett.* **1985**, *55*, 1768.
[23] G. Zeng, J. E. Bowers, Y. Zhang, A. Shakouri, J. Zide, A. Gossard, W. Kim, A. Majumdar, in *24th Int. Conf. Thermoelectr.*, IEEE, Piscataway, NJ **2005**, pp. 500–503.
[24] M. Garbrecht, I. Mccarroll, L. Yang, V. Bhatia, B. Biswas, D. Rao, J. M. Cairney, B. Saha, *J. Mater. Sci.* **2020**, *55*, 1592.
[25] J. L. Schroeder, B. Saha, M. Garbrecht, N. Schell, T. D. Sands, J. Birch, *J. Mater. Sci.* **2015**, *50*, 3200.
[26] B. Saha, S. K. Lawrence, J. L. Schroeder, J. Birch, D. F. Bahr, T. D. Sands, *Appl. Phys. Lett.* **2014**, *105*, 151904.
[27] H. N. S. Krishnamoorthy, Z. Jacob, E. Narimanov, I. Kretzschmar, V. M. Menon, *Science.* **2012**, *336*, 205.
[28] M. Y. Shalaginov, V. V. Vorobyov, J. Liu, M. Ferrera, A. V. Akimov, A. Lagutchev, A. N. Smolyaninov, V. V. Klimov, J. Irudayaraj, A. V. Kildishev, A. Boltasseva, V. M. Shalaev, *Laser Photon. Rev.* **2015**, *9*, 120.
[29] M. Zebarjadi, Z. Bian, R. Singh, A. Shakouri, R. Wortman, V. Rawat, T. Sands, *J. Electron. Mater.* **2009**, *38*, 960.
[30] K. Upadhya, D. Rao, B. Biswas, R. Kumar, V. Bhatia, A. I. K. Pillai, M. Garbrecht, B. Saha, *Appl. Phys. Lett.* **2021**, *118*, 202107.
[31] K. C. Maurya, B. Biswas, D. Rao, B. Saha, *Appl. Phys. Lett.* **2021**, *118*, 041902.

[32] R. Ahuja, J. M. Wills, B. Johansson, O. Eriksson, *Phys. Rev. B.* **1993**, *48*, 16269.
[33] X. Bai, Y. Li, B. Xiao, Y. Rao, H. Liang, L. He, J. Feng, *Mater. Chem. Phys.* **2020**, *254*, 123423.
[34] A. Grillo, A. Di Bartolomeo, *Adv. Electron. Mater.* **2021**, *7*, 2000979.
[35] S. M. Sze, K. K. Ng, *Physics of Semiconductor Devices*, Wiley, New York, Chichester, UK **2006**.
[36] J. Hölzl, F. K. Schulte, H. Wagner, *Solid Surf. Phys*, Springer-Verlag, Berlin, Heidelberg **1979**, 124.
[37] B. L. Ward, J. D. Hartman, E. H. Hurt, K. M. Tracy, R. F. Davis, R. J. Nemanich, *J. Vac. Sci. Technol. B.* **2000**, *18*, 2082.
[38] C. I. Wu, A. Kahn, E. S. Hellman, D. N. E. Buchanan, *Appl. Phys. Lett.* **1998**, *73*, 1346.
[39] R. T. Tung, *Appl. Phys. Rev.* **2014**, *1*, 011304.
[40] T. J. Drummond, *Phys. Rev. B.* **1999**, *59*, 8182.
[41] P. Reddy, I. Bryan, Z. Bryan, J. Tweedie, R. Kirste, R. Collazo, Z. Sitar, *J. Appl. Phys.* **2014**, *116*, 194503.
[42] A. Jadhav, L. A. M. Lyle, Z. Xu, K. K. Das, L. M. Porter, B. Sarkar, *J. Vac. Sci. Technol. B.* **2021**, *39*, 040601.
[43] J. H. Werner, H. H. Güttler, *J. Appl. Phys.* **1991**, *69*, 1522.
[44] H. Li, D. He, Q. Zhou, P. Mao, J. Cao, L. Ding, J. Wang, *Sci. Rep.* **2017**, *7*, 40134.
[45] W. Lim, J.-H. Jeong, J.-H. Lee, S.-B. Hur, J.-K. Ryu, K.-S. Kim, T.-H. Kim, S. Y. Song, J.-I. Yang, S. J. Pearton, *Appl. Phys. Lett.* **2010**, *97*, 242103.
[46] C. Wenger, M. Lukosius, G. Weidner, H. J. Müssig, S. Pasko, C. Lohe, *Thin Solid Films.* **2009**, *517*, 6334.
[47] P. Gonon, C. Valláe, *Appl. Phys. Lett.* **2007**, *90*, 142906.
[48] S. Mondal, S. J. Shih, F. H. Chen, T. M. Pan, *IEEE Trans. Electron Devices.* **2012**, *59*, 1750.
[49] D. Vashaee, A. Shakouri, *Phys. Rev. Lett.* **2004**, *92*, 106103.
[50] G. Zeng, J. M. O. Zide, W. Kim, J. E. Bowers, A. C. Gossard, Z. Bian, Y. Zhang, A. Shakouri, S. L. Singer, A. Majumdar, *J. Appl. Phys.* **2007**, *101*, 034502.
[51] G. D. Mahan, L. M. Woods, *Phys. Rev. Lett.* **1998**, *80*, 4016.
[52] J.-H. Bahk, A. Shakouri, in *2019 IEEE BiCMOS Compd. Semicond. Integr. Circuits Technol. Symp*, IEEE, Piscataway, NJ **2019**, 1.
[53] B. Xu, M. Di Gennaro, M. J. Verstraete, *Phys. Rev. B.* **2020**, *102*, 155128.
[54] J. Sonntag, *J. Phys. Condens. Matter.* **2010**, *22*, 235501.